

# Discrete-time Sliding Mode Observer for Sensorless Vector Control of Permanent Magnet Synchronous Machine

Thiago Bernardes, Vinícius Foleto Montagner, Hilton Abílio Gründling, Humberto Pinheiro, *Member, IEEE*

**Abstract**—This paper proposes a sensorless vector control that combines two discrete-time observers to estimate the rotor speed and position of permanent magnet synchronous machines (PMSM). The first one is a sliding mode (DSM) current observer and the second one is an adaptive electromotive force (EMF) observer. Initially, the sliding conditions that assure the sliding motion around the sliding surface are derived and a design procedure to the DSM current observer is developed. Moreover, using discrete-time adaptive Lyapunov based EMF observer the rotor speed and position are obtained. Experimental results validate the theoretical analysis and demonstrate the very good performance of the proposed discrete-time sensorless vector control.

**Keywords**—Sensorless vector control, discrete-time sliding mode, Lyapunov's direct method, current observer, adaptive EMF observer.

## I. INTRODUCTION

IN recent years, researchers and industries have been paying attention to permanent magnet synchronous machines (PMSM) because of their high efficiency, high power-weight ratio and simple structure compared with others machines. High performance electrical drives using PMSM require the knowledge of the rotor position to implement the field oriented control. Mechanical sensors can provide the information for the rotor position, however they increase the cost and decrease the reliability of the drive. Besides, mechanical sensors are susceptible to fail in harmful environment conditions [1]. Hence, sensorless control techniques provide the means to overcome the above mentioned limitations.

Sensorless control techniques can be divided into two classes [1]–[3]. The first one are based on the signal injection [4]–[8],

Manuscript submitted November 29, 2012; revised February 20, 2013 and April 08, 2013 and May 14, 2013. Accepted for publication May 24, 2013. This work was supported in part by Coordenação de Aperfeiçoamento de Pessoal de Nível Superior (CAPES) and in part by National Counsel of Technological and Scientific Development (CNPq).

Copyright (c) 2009 IEEE. Personal use of this material is permitted. However, permission to use this material for any other purposes must be obtained from the IEEE by sending a request to [pubs-permissions@ieee.org](mailto:pubs-permissions@ieee.org).

T. Bernardes is with the Power Electronics and Control Research Group (GEPoC), Federal University of Santa Maria (UFSM), 97105-900 Santa Maria, Brazil (e-mail: thiagobernardes83@gmail.com).

V. F. Montagner, H. A. Gründling and H. Pinheiro are with Department of Electrical Energy Conversion (DPEE), Federal University of Santa Maria (UFSM), 97105-900 Santa Maria, Brazil.

while the second one on the fundamental excitation [9]–[27]. The former explores the rotor anisotropies from high frequency (HF) signals that are injected into the machine. This method allows operation at low speed and at standstill. However, the injected signals can produce harmonic currents, which increase electrical losses and induce torque oscillations. The latter depends on the machine model to estimate its electromotive force (EMF), which, in turn, can provide the information of the rotor position and speed. This method is suitable for medium and high speed range and remains the standard industrial solution [3].

Regarding the fundamental excitation method, Wu and Slemmon [9] estimate the EMF using the voltage and current measures from operational amplifiers by integration, which can degrade the accuracy of the estimation. Bolognani *et al.* [10] use an extended Kalman filter with online tuning of the rotor flux. Although this solution provides wide speed range and has been shown to be capable of delivering full torque at standstill, it requires a high computational effort to compute the optimum state estimation gain matrix from the covariance matrix at every control cycle. Rashed *et al.* [11] describe a sensorless indirect-rotor-field-oriented, which addresses the noise sensitive and the stator resistance mismatch. The rotor speed and stator resistance or rotor speed and rotor-flux magnitude are estimated using model reference adaptive systems. It has been shown that the rotor speed and stator resistance scheme has a better performance at low-speed operation, while rotor speed and rotor-flux magnitude estimation is most appropriate for high-speed range. Lian *et al.* [12] propose a sensorless speed control scheme based on Takagi-Sugeno fuzzy model where its design uses linear matrix inequalities. The results reveal that it can operate at low speed. Piippo *et al.* [13] combine the fundamental excitation with the signal injection technique using an observer by model reference adaptive system. This solution improves the operation at low speed range, however torque ripple can appear owing to the injected signals. Singh and Chandra [14] estimate the rotor speed and position using a neuro-fuzzy adaptive observer. The experiments show an effective performance considering a wind turbine application. Ortega *et al.* [15] propose a nonlinear position observer. A thorough stability analysis is carried out in continuous-time domain and it is shown that, depending on the load condition, the system performance degrades when the speed approaches zero. On the other hand, [16]–[26], [28]–[30] propose sensorless control using sliding mode (SM)

approach. The main reasons to use SM are: reduced order, simple implementation and inherent robustness in the presence of parameter uncertainties and of perturbations [31], [32], which are attractive advantages. It is important to point out that the design and stability analysis of the observers are usually carried out in continuous-time domain, while their implementations are in discrete-time domain. Thus, the continuous-time sliding mode conditions can fail to predict stability performance of the system [33], [34].

This paper proposes a sensorless vector control for surface permanent magnet synchronous machines entirely in the discrete-time domain. First, a discrete-time sliding mode current observer provides an estimation of the electromotive force vector. The sliding conditions are established to assure the quasi-sliding motion in discrete-time and a design procedure is proposed to minimize the chattering. Then, a discrete-time adaptive electromotive force observer is proposed based on Lyapunov's direct method, which yields the rotor position and speed. Among the contributions of this paper are the design procedure and the analysis that are carried out in discrete-time domain making it suitable for a microcontroller or DSP implementation. In addition, the experimental results support the theoretical analysis.

This paper is organized as follows. Section II presents the PMSM models. Section III discloses the proposed discrete-time speed and position observer, which comprises: the discrete-time sliding mode current observer, adaptive EMF observer. In addition, the stability analysis and the design methodology is also presented in the section. Section IV describes the current controller. Section V shows the experimental results to validate the proposed sensorless vector control. Section VI concludes the paper.

## II. PMSM MODELS

This section derives continuous and discrete dynamic models for nonsalient PMSM in stationary ( $\alpha\beta$ ) reference frame. The nominal model considers a sinusoidal flux distribution machine without saturation.

### A. Continuous-time model

The continuous-time dynamic behaviour of a nonsalient PMSM in stationary reference frame can be expressed as

$$\dot{\mathbf{i}}_{\alpha\beta} = \Phi \mathbf{i}_{\alpha\beta} + \Gamma \mathbf{v}_{\alpha\beta} - \Gamma \mathbf{e}_{\alpha\beta} \quad (1)$$

where

$$\mathbf{i}_{\alpha\beta} = [i_\alpha \ i_\beta]^T, \quad \mathbf{v}_{\alpha\beta} = [v_\alpha \ v_\beta]^T \text{ and } \mathbf{e}_{\alpha\beta} = [e_\alpha \ e_\beta]^T$$

denote the vectors of stator currents and voltages, and induced electromotive force (EMF). The matrices  $\Phi$  and  $\Gamma$  are given by

$$\Phi = \begin{bmatrix} -\frac{R_s}{L_s} & 0 \\ 0 & -\frac{R_s}{L_s} \end{bmatrix} \quad \text{and} \quad \Gamma = \begin{bmatrix} \frac{1}{L_s} & 0 \\ 0 & \frac{1}{L_s} \end{bmatrix}$$

with  $R_s$  and  $L_s$  being the stator resistance and inductance. The rotor flux can be written as

$$\psi_{\alpha\beta}^r = \psi_{pm} \begin{bmatrix} \cos \theta_e \\ \sin \theta_e \end{bmatrix}$$

where  $\psi_{pm}$  and  $\theta_e$  are the magnet flux and the rotor position. Hence, the electromotive force (EMF) become

$$\mathbf{e}_{\alpha\beta} = \omega_e \psi_{pm} \begin{bmatrix} -\sin \theta_e \\ \cos \theta_e \end{bmatrix} \quad (2)$$

where  $\omega_e$  is the rotor speed. Therefore, the behaviour of the EMF can be expressed as

$$\dot{\mathbf{e}}_{\alpha\beta} = \omega_e \mathbf{J} \mathbf{e}_{\alpha\beta} \quad (3)$$

where

$$\mathbf{J} = \begin{bmatrix} 0 & -1 \\ 1 & 0 \end{bmatrix}, \quad (4)$$

if the rotor speed, which depends on the mechanical dynamics, varies slowly in relation to the electrical variables (currents, fluxes and voltages), i.e.,  $\dot{\omega}_e \approx 0$ .

### B. Discrete-time model

To develop the proposed discrete-time sensorless vector control, (1) can be discretized as

$$\mathbf{i}_{\alpha\beta(k+1)} = \mathbf{A} \mathbf{i}_{\alpha\beta(k)} + \mathbf{B} \mathbf{v}_{\alpha\beta(k)} - \mathbf{B} \mathbf{e}_{\alpha\beta(k)} \quad (5)$$

where

$$\mathbf{A} = e^{\Phi T_s} \quad \text{and} \quad \mathbf{B} = \int_0^{T_s} e^{\Phi \tau} \mathbf{\Gamma} d\tau,$$

and  $T_s$  is the sampling period. The discretization of (3) results in the difference equation that described the behaviour of the EMF, that is

$$\mathbf{e}_{\alpha\beta(k+1)} = \mathbf{e}_{\alpha\beta(k)} + T_s \omega_e(k) \mathbf{J} \mathbf{e}_{\alpha\beta(k)}. \quad (6)$$

In the following section, the discrete-time speed and position observer is proposed for the nonsalient PMSM using (5) and (6).

## III. DISCRETE-TIME SPEED AND POSITION OBSERVER

This section discloses the proposed discrete-time speed and position observer, which comprises two blocks. The first one consists in a discrete-time sliding mode (DSM) current observer, which provides a reference of EMF for the discrete-time adaptive EMF observer whose outputs are the estimated rotor speed and position, as shown Fig. 1.

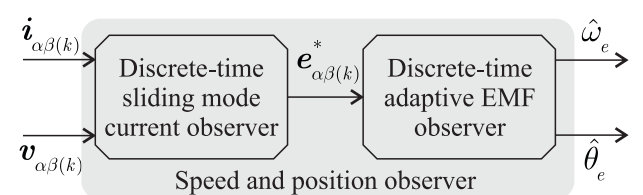


Fig. 1. Block diagram of proposed discrete-time speed and position observer.

The following subsections describe in details, prove the stability and provide a design procedure for DSM current observer aiming to assure the quasi-sliding mode in discrete-time domain under a limited sampling frequency.

### A. Discrete-time sliding mode current observer

The discrete-time sliding mode (DSM) current observer is proposed as

$$\hat{\mathbf{i}}_{\alpha\beta(k+1)} = \mathbf{A}\hat{\mathbf{i}}_{\alpha\beta(k)} + \mathbf{B}\mathbf{v}_{\alpha\beta(k)} - \mathbf{B}\mathbf{u}_{\alpha\beta(k)} \quad (7)$$

where  $\hat{\mathbf{i}}_{\alpha\beta(k)}$  is the estimated current,  $\mathbf{u}_{\alpha\beta(k)}$  defines an attraction function as

$$\mathbf{u}_{\alpha\beta(k)} = \mathbf{e}_{\alpha\beta(k)}^{\text{eq}} + (\mathbf{B}^{-1}\mathbf{AB} + h_1\mathbf{I})\sigma_{\alpha\beta(k)} + h_2\mathbf{I}\text{sign}(\sigma_{\alpha\beta(k)}), \quad (8)$$

$h_1$  and  $h_2$  are positive constants,  $\text{sign}()$  denotes the sign function,  $\mathbf{e}_{\alpha\beta(k)}^{\text{eq}}$  amounts to actual EMF, and  $\sigma_{\alpha\beta(k)}$  is a sliding function defined as

$$\sigma_{\alpha\beta(k)} = \mathbf{B}^{-1}\tilde{\mathbf{i}}_{\alpha\beta(k)} \quad (9)$$

with  $\tilde{\mathbf{i}}_{\alpha\beta(k)}$  being the error between  $\hat{\mathbf{i}}_{\alpha\beta(k)}$  and  $\mathbf{i}_{\alpha\beta(k)}$ .

Fig. 2 shows the DSM current observer block diagram, which has a low-pass filter (LPF2) to reduce the chattering amplitude at half sampling frequency.

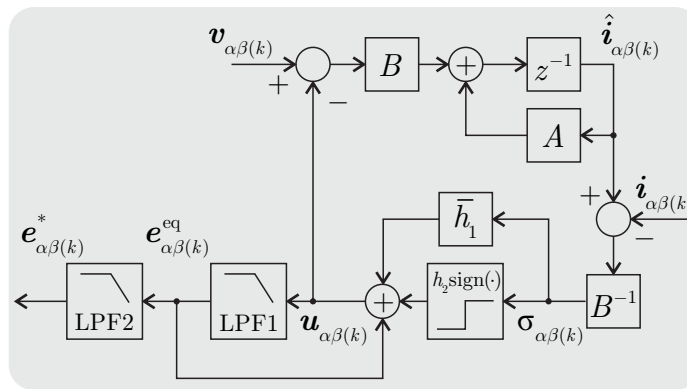


Fig. 2. Block diagram of the discrete-time sliding mode current observer where  $\bar{h}_1 = (\mathbf{B}^{-1}\mathbf{AB} + h_1\mathbf{I})$ .

To ensure the convergence of the observer (7), the sliding conditions shall be verified in the discrete-time domain. Sarp-turk's DSM [33] proposes the inequalities

$$(\sigma_{i(k+1)} - \sigma_{i(k)})\text{sign}(\sigma_{i(k)}) < 0 \quad (10)$$

$$(\sigma_{i(k+1)} + \sigma_{i(k)})\text{sign}(\sigma_{i(k)}) \geq 0 \quad (11)$$

to assure both quasi-sliding motion and convergence onto the  $i$ th surface. The inequality (10) guarantees that the state trajectories point toward in a sliding surfaces  $\sigma_i = 0$ . On the other hand, the inequality (11) ensures that the chattering amplitude of the state trajectories decreases towards  $\sigma_i = 0$  or it remains limited to a sliding band. These inequalities are known as the sliding and the convergence conditions. An alternative for (11) is

$$-\sigma_{i(k+1)}\text{sign}(\sigma_{i(k)}) \leq \sigma_{i\max}, \quad (12)$$

for  $|\sigma_{i(k)}| \leq \sigma_{i\max}$  where  $\sigma_{i\max}$  is the sliding mode band. Therefore, whenever (10) and (12) are assured the state trajectories will enter and remain within the region defined by the sliding mode band  $\sigma_{i\max}$ .

The following Theorem establishes the bounds for the DSM current observer gains to ensure quasi-sliding motion.

**Theorem 1** Consider the current observer (7) subjected to the sliding function (9) and to the attraction function (8) where the low-pass filter 1 (LPF1) is neglected. The sliding function converges and remains in an attraction region around the surface  $\sigma_i = 0$  for a known  $\sigma_{i\max}$  where  $|\sigma_{i(k)}| \leq \sigma_{i\max}$ ,  $i = \alpha, \beta$ , if the positive gain  $h_2$  satisfies

$$\max([1 \ -1 - h_1]\mathbf{M}) \leq h_2 < \min([1 \ 1 - h_1]\mathbf{M})$$

where

$$\mathbf{M} = \begin{bmatrix} \tilde{e}_{\alpha\max} & \tilde{e}_{\beta\max} \\ \sigma_{\alpha\max} & \sigma_{\beta\max} \end{bmatrix} \quad (13)$$

for some positive gain  $h_1$  with  $\tilde{e}_{\alpha\beta(k)}$  being the error between  $\mathbf{e}_{\alpha\beta(k)}^{\text{eq}}$  and  $\mathbf{e}_{\alpha\beta(k)}$  where  $|\tilde{e}_{i(k)}| \leq \tilde{e}_{i\max}$  is its upper bound.  $\diamond$

*Proof:* The difference equation of the estimated current error is obtained by subtracting (5) of (7), that is

$$\tilde{\mathbf{i}}_{\alpha\beta(k+1)} = \mathbf{A}\tilde{\mathbf{i}}_{\alpha\beta(k)} + \mathbf{B}\mathbf{e}_{\alpha\beta(k)} - \mathbf{B}\mathbf{u}_{\alpha\beta(k)}. \quad (14)$$

Hence, the dynamic behaviour of the sliding function can be derived from (8), (9) and (14) as

$$\sigma_{\alpha\beta(k+1)} = -\tilde{e}_{\alpha\beta(k)} - h_1\mathbf{I}\sigma_{\alpha\beta(k)} - h_2\mathbf{I}\text{sign}(\sigma_{\alpha\beta(k)}). \quad (15)$$

The conditions (10) and (12) for  $\alpha$ -axis component that assure quasi-sliding motion and convergence to the sliding mode band are

$$-(1 + h_1)|\sigma_{\alpha(k)}| - \tilde{e}_{\alpha(k)}\text{sign}(\sigma_{\alpha(k)}) - h_2 < 0 \quad (16)$$

$$h_1|\sigma_{\alpha(k)}| + \tilde{e}_{\alpha(k)}\text{sign}(\sigma_{\alpha(k)}) + h_2 \leq \sigma_{\alpha\max}. \quad (17)$$

By manipulating (16) and (17) results

$$\tilde{e}_{\alpha\max} - (1 + h_1)\sigma_{\alpha\max} < h_2 \leq \tilde{e}_{\alpha\max} + (1 - h_1)\sigma_{\alpha\max} \quad (18)$$

if  $\tilde{e}_{\alpha(k)}$  and  $\sigma_{\alpha(k)}$  differ in their signs. A similar result can be obtained for  $\beta$ -axis component. Hence, it is possible to infer that if

$$\max([1 \ -1 - h_1]\mathbf{M}) < h_2 \leq \min([1 \ 1 - h_1]\mathbf{M}) \quad (19)$$

for some positive gain  $h_1$ , then the sliding function converges and remains in an attraction region around the  $\sigma_i = 0$  where  $\sigma_{i\max}$  is the sliding mode band.  $\blacksquare$

Theorem 1 disregards the LPF1 dynamics, which can affect the observer stability. Then, in the following, its dynamic is included in the analysis.

The dynamic equation of the LPF1 is described by

$$\mathbf{e}_{\alpha\beta(k+1)}^{\text{eq}} = (1 - T_s\omega_{\text{cut}})\mathbf{I}\mathbf{e}_{\alpha\beta(k)}^{\text{eq}} + T_s\omega_{\text{cut}}\mathbf{I}\mathbf{u}_{\alpha\beta(k)} \quad (20)$$

where  $\omega_{\text{cut}}$  is the cutoff frequency. By using the attraction function (8) it becomes

$$\mathbf{e}_{\alpha\beta(k+1)}^{\text{eq}} = \mathbf{e}_{\alpha\beta(k)}^{\text{eq}} + h_4\sigma_{\alpha\beta(k)} + h_5\text{sign}(\sigma_{\alpha\beta(k)}) \quad (21)$$

where

$$h_4 = T_s\omega_{\text{cut}}(\mathbf{B}^{-1}\mathbf{AB} + h_1\mathbf{I}) \text{ and } h_5 = T_s\omega_{\text{cut}}h_2\mathbf{I}.$$

Hence, considering one axis component, the dynamic equations for the sliding function (15) and for the EMF (21) are

$$\begin{bmatrix} \sigma_{(k+1)} \\ \tilde{e}_{(k+1)} \end{bmatrix} = \begin{bmatrix} -h_1 & -1 \\ h_4 & 1 \end{bmatrix} \begin{bmatrix} \sigma_{(k)} \\ \tilde{e}_{(k)} \end{bmatrix} + \begin{bmatrix} -h_2 & 0 \\ h_5 & -1 \end{bmatrix} \begin{bmatrix} \text{sign}(\sigma_{(k)}) \\ \Delta e_{(k)} \end{bmatrix} \quad (22)$$

that describes dynamic behaviour of the DSM current observer with the LPF1. In (22),  $\Delta e_{(k)} = e_{(k+1)} - e_{(k)}$  denotes the difference between two successive samples of actual EMF and  $\tilde{e}_{(k)}$  is the estimation error of EMF. Equation (22) can written in a compact form as

$$\mathbf{x}(k+1) = \mathbf{G}\mathbf{x}(k) + \mathbf{H}_i + \mathbf{H}_2 w_{(k)} \quad (23)$$

where the vector  $\mathbf{x}(k) = [\sigma_{(k)} \ \tilde{e}_{(k)}]^T$  and the perturbation  $w_{(k)}$  is  $\Delta e_{(k)}$ , and the matrices  $\mathbf{G}$ ,  $\mathbf{H}_2$  and  $\mathbf{H}_i$  are

$$\mathbf{G} = \begin{bmatrix} -h_1 & -1 \\ h_4 & 1 \end{bmatrix}, \quad \mathbf{H}_2 = \begin{bmatrix} 0 \\ -1 \end{bmatrix} \text{ and} \\ \mathbf{H}_i = \begin{cases} \mathbf{H}_{1\sigma_+} = \begin{bmatrix} -h_2 & h_5 \end{bmatrix}^T & \text{if } \sigma_{(k)} > 0, \\ \mathbf{H}_{1\sigma_-} = \begin{bmatrix} h_2 & -h_5 \end{bmatrix}^T & \text{if } \sigma_{(k)} < 0. \end{cases} \quad (24)$$

The bounded input sequence  $([1 \ w_{(k)}]^T)$  forces the switching linear system (23). Thus, if matrix  $\mathbf{G}$  is Schur, then (23) is BIBO stable [35], [36]. Hence, the stability of the DSM current observer is assured. Moreover, a design procedure can be developed from the above equations.

### B. Design procedure of the DSM current observer

Poincaré maps are used to determine the stability of periodic solutions of continuous differential equations from the stability of a fixed point solution of a lower order difference equation [37]–[39]. Similarly, here the dynamic behavior of (23), which exhibits a quasi-sliding motion, will be analyzed from the map of  $\mathbf{x}(k) \rightarrow \mathbf{x}(k+2)$ . This map results in a linear discrete equation that provides the evolution of the estimation error  $\tilde{e}_{(k)}$  and of the sliding function  $\sigma_{(k)}$  from the  $k^{th}$  to the  $(k+2)^{th}$  sampling instant. Thus, a design methodology is proposed to decrease the chattering effects and to assure the quasi-sliding motion around the surface  $\sigma = 0$  for the DSM current observer (7).

The quasi-sliding motion attributes establish that the desired state trajectories shall intersect the switching plane in successive sampling period after the first cross [40]. Considering (23) and defining a sliding plane  $x = 0$ , then the quasi-sliding motion becomes as shown in Fig. 3, which shall be assured for a bounded perturbation  $w_{(k)}$ .

To investigate the behaviour of the sliding motion, the difference equations that maps  $\mathbf{x}(k)$  into  $\mathbf{x}(k+2)$  is obtained by

$$\begin{aligned} \mathbf{x}(k+1) &= \mathbf{G}\mathbf{x}(k) + \mathbf{H}_{1\sigma_-} + \mathbf{H}_2 w_{(k)} \\ \mathbf{x}(k+2) &= \mathbf{G}\mathbf{x}(k+1) + \mathbf{H}_{1\sigma_+} + \mathbf{H}_2 w_{(k+1)} \end{aligned}$$

resulting in

$$\mathbf{x}(k+2) = \mathbf{G}^2 \mathbf{x}(k) + \mathbf{G}\mathbf{H}_{1\sigma_-} + \mathbf{H}_{1\sigma_+} + [\mathbf{G}\mathbf{H}_2 \quad \mathbf{H}_2] \begin{bmatrix} w_{(k)} \\ w_{(k+1)} \end{bmatrix}. \quad (25)$$

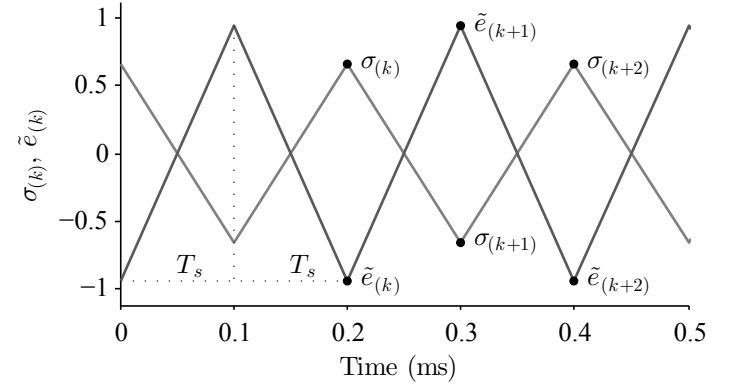


Fig. 3. State trajectory of the  $\sigma_{(k)}$  in discrete-time for  $w_{(k)} = 0$ .

The equilibrium point of (25) and the impact of perturbation  $w_{(k)}$  determine the chattering amplitude. Initially, the equilibrium point of (25),  $\mathbf{x}^* = (\sigma^*, \tilde{e}^*)$ , is obtained making  $w_{(k)} = 0$ , that is

$$\mathbf{x}^* = (\mathbf{I} - \mathbf{G}^2)^{-1} (\mathbf{G}\mathbf{H}_{1\sigma_-} + \mathbf{H}_{1\sigma_+}). \quad (26)$$

Then, the impact of  $w_{(k)}$  is determined from the transfer function

$$\mathbf{x}_{(z)} = (z^2 \mathbf{I} - \mathbf{G}^2)^{-1} (\mathbf{G}\mathbf{H}_2 + z\mathbf{H}_2) w_{(z)}. \quad (27)$$

Hence, the maximum absolute value of the components of  $\mathbf{x}(k)$  are given by

$$\sigma_{\max} = |\sigma^*| + g_1 |w_{(k)}|_{\max} \quad (28)$$

$$\tilde{e}_{\max} = |\tilde{e}^*| + g_2 |w_{(k)}|_{\max} \quad (29)$$

that characterize the chattering amplitude. The transfer function (27) provides the gains

$$g_1 = \left| \frac{\sigma(z)}{w(z)} \right| \quad \text{and} \quad g_2 = \left| \frac{\tilde{e}(z)}{w(z)} \right|,$$

and  $|w_{(k)}|_{\max}$  denotes the maximum absolute value of  $w_{(k)}$ , which depends on the sampling frequency and on the application. Fig. 4 shows the  $|w_{(k)}|_{\max}$  versus the sampling frequency for a permanent magnet synchronous machine (PMSM) with sinusoidal EMF.

Moreover, the conditions

$$\begin{aligned} |\sigma^*| - g_1 |w_{(k)}|_{\max} &> 0 \text{ and} \\ |\tilde{e}^*| - g_2 |w_{(k)}|_{\max} &> 0 \end{aligned} \quad (30)$$

are proposed and they assure quasi-sliding motion, as shown Fig. 3, under bounded perturbation  $w_{(k)}$ .

The design procedure to compute the gains  $h_1$  and  $h_2$ , and the cutoff frequency  $\omega_{\text{cut}}$  has to ensure that even under the perturbation  $w_{(k)}$  the quasi-sliding motion attributes are assured. A two steps define design procedure is proposed here. The first step computes the gain  $h_1$  and the cutoff frequency  $\omega_{\text{cut}}$ , assuming the maximum value of perturbation  $w_{(k)}$ , as follows:

- (i) define a range for the gain  $h_1$  and the cutoff frequency  $\omega_{\text{cut}}$  as well as a region inside of the unit circle for the eigenvalues of  $\mathbf{G}^2$ ;

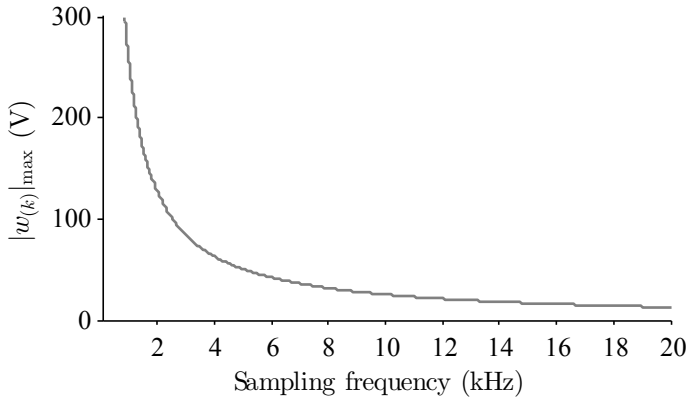


Fig. 4. Amplitude of the  $w_{(k)}$  versus sampling frequency for the nominal operating of a PMSM at 160 Hz with 12 pole pairs.

- (ii) compute the gains  $g_1$  and  $g_2$  for each pair  $(h_1, \omega_{\text{cut}})$ ;
- (iii) select among the pairs  $(h_{1\text{opt}}, \omega_{\text{cutopt}})$  that results in the eigenvalues of  $\mathbf{G}^2$  inside the defined region the one that provides the smallest sum of  $g_1$  and  $g_2$ .

The second step determines the gain  $h_2$ , for the pair  $(h_{1\text{opt}}, \omega_{\text{cutopt}})$ , as follows:

- (i) define a range of the  $h_2$ ;
- (ii) compute the equilibrium  $(\sigma^*, \tilde{e}^*)$  for each  $h_2$ ;
- (iii) compute the values  $\sigma_{\text{max}}$  and  $\tilde{e}_{\text{max}}$ ;
- (iv) verify the inequalities (30), and
- (v) choose the gain  $h_{2\text{opt}}$  that results in the smallest sum of  $\sigma_{\text{max}}$  and  $\tilde{e}_{\text{max}}$ .

Therefore, if the gains and the cutoff frequency are determined according to the above procedure, then the conditions of Theorem 1 are satisfied. This methodology is exemplified in an pseudo-code in Appendix A. The LPF2 bandwidth shall be chosen to attenuate the chattering high frequency components, providing a reference EMF vector  $e_{\alpha\beta(k)}^*$  that is the input for the discrete-time adaptive EMF observer whose the outputs are the estimated rotor speed and position.

### C. Discrete-time adaptive EMF observer

This section describes the discrete-time adaptive EMF observer using Lyapunov's Direct Method. Fig. 5 shows the adaptive observer block diagram.

The dynamic behaviour (6) for EMF can be written as

$$e_{\alpha\beta(k+1)} = e_{\alpha\beta(k)} + T_s \omega_{e(k+1)} \mathbf{J} e_{\alpha\beta(k)}, \quad (31)$$

where the electric speed  $\omega_{e(k)}$  has been considered to vary slowly between two successive samples, i.e.,  $\Delta\omega_{e(k)} \approx 0$ . Hence, the EMF observer can be defined by

$$\hat{e}_{\alpha\beta(k+1)} = \hat{e}_{\alpha\beta(k)} + T_s \hat{\omega}_{e(k+1)} \mathbf{J} e_{\alpha\beta(k)} - h_3 \tilde{e}_{\alpha\beta(k)} \quad (32)$$

where  $h_3$  and  $\hat{\omega}_{e(k+1)}$  denote a constant gain and the estimated rotor speed one step ahead, and  $\tilde{e}_{\alpha\beta(k)} = \hat{e}_{\alpha\beta(k)} - e_{\alpha\beta(k)}$  is the EMF estimated error, where the reference EMF  $e_{\alpha\beta(k)}^*$  equals the actual EMF  $e_{\alpha\beta(k)}$ .

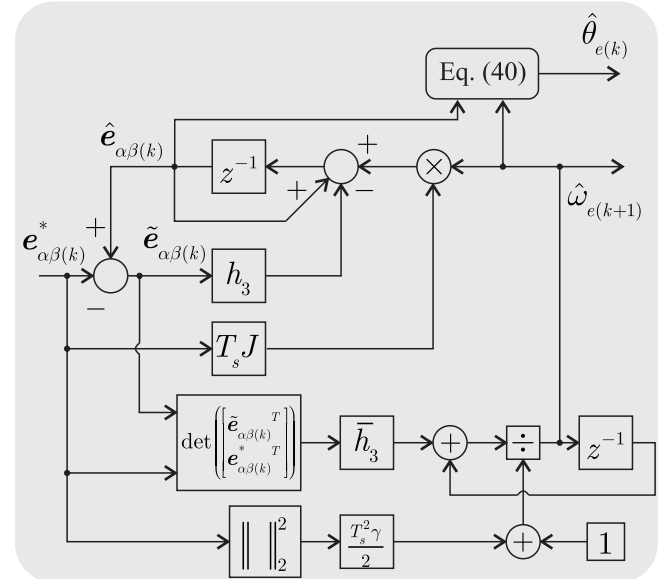


Fig. 5. Block diagram of the discrete-time adaptive EMF observer where  $\bar{h}_3 = T_s \gamma (1 - h_3)$ .

The following Theorem defines the adaptive law to estimate the rotor speed.

**Theorem 2** Assuming  $\omega_{e(k)}$  varies slowly between two successive samples and an adaptive law that results in the following speed estimation error

$$\tilde{\omega}_{e(k+1)} = \frac{\tilde{\omega}_{e(k)}}{1 + \frac{T_s}{2}\gamma \left\| e_{\alpha\beta(k)} \right\|_2^2} - \frac{T_s \gamma (1 - h_3) (\tilde{e}_{\alpha\beta(k)}^T \mathbf{J} e_{\alpha\beta(k)})}{1 + \frac{T_s^2}{2}\gamma \left\| e_{\alpha\beta(k)} \right\|_2^2} \quad (33)$$

where  $\gamma$  denotes a positive gain. Hence, if the gain  $h_3$  belongs to the range  $(0, 2)$ , then the estimated EMF  $\hat{e}_{\alpha\beta(k)}$  and speed  $\tilde{\omega}_{e(k)}$  converge to their actual values  $e_{\alpha\beta(k)}$  and  $\omega_{e(k)}$ .  $\diamond$

*Proof:* The difference equation (31) and (32) are subtracted to provide the dynamic behaviour of the estimated EMF error given by

$$\tilde{e}_{\alpha\beta(k+1)} = (1 - h_3) I \tilde{e}_{\alpha\beta(k)} + T_s \tilde{\omega}_{e(k+1)} \mathbf{J} e_{\alpha\beta(k)} \quad (34)$$

where  $\tilde{\omega}_{e(k)} = \hat{\omega}_{e(k)} - \omega_{e(k)}$  denotes estimated speed error. In addition, the candidate Lyapunov function

$$V_{(k)} = \tilde{e}_{\alpha\beta(k)}^T \tilde{e}_{\alpha\beta(k)} + \gamma^{-1} \tilde{\omega}_{e(k)}^2 \quad (35)$$

is chosen where  $\gamma$  is positive constant. Then, the forward difference of the Lyapunov function (35) can be written by

$$\Delta V_{(k)} = \tilde{e}_{\alpha\beta(k+1)}^T \tilde{e}_{\alpha\beta(k+1)} - \tilde{e}_{\alpha\beta(k)}^T \tilde{e}_{\alpha\beta(k)} + \gamma^{-1} (\tilde{\omega}_{e(k+1)}^2 - \tilde{\omega}_{e(k)}^2), \quad (36)$$

that must be negative to guarantee the stability of the adaptive EMF observer. Moreover, the estimated speed error variation is defined by  $\Delta\tilde{\omega}_{e(k)} = \tilde{\omega}_{e(k+1)} - \tilde{\omega}_{e(k)}$  that leads to

$$\tilde{\omega}_{e(k+1)}^2 - \tilde{\omega}_{e(k)}^2 = -\Delta\tilde{\omega}_{e(k)}^2 + 2\Delta\tilde{\omega}_{e(k)}\tilde{\omega}_{e(k+1)}.$$

Hence, the Lyapunov function variation (36) becomes

$$\begin{aligned}\Delta V_{(k)} = & [(1 - h_3)^2 - 1] \left\| \tilde{\mathbf{e}}_{\alpha\beta(k)} \right\|_2^2 - \gamma^{-1} \Delta \tilde{\omega}_{e(k)}^2 \\ & + 2T_s (1 - h_3) \tilde{\omega}_{e(k+1)} \tilde{\mathbf{e}}_{\alpha\beta(k)}^T \mathbf{J} \mathbf{e}_{\alpha\beta(k)} + \\ & + T_s^2 \left\| \mathbf{e}_{\alpha\beta(k)} \right\|_2^2 \tilde{\omega}_{e(k+1)}^2 + 2\gamma^{-1} \Delta \tilde{\omega}_{e(k)} \tilde{\omega}_{e(k+1)},\end{aligned}\quad (37)$$

resulting in

$$\Delta V_{(k)} = [(1 - h_3)^2 - 1] \left\| \tilde{\mathbf{e}}_{\alpha\beta(k)} \right\|_2^2 - \gamma^{-1} \Delta \tilde{\omega}_{e(k)}^2 \quad (38)$$

from the adaptive law (33).

In conclusion, if the gain  $h_3$  belongs to the range  $(0, 2)$ , then (38) is negative. Therefore, the  $\tilde{\mathbf{e}}_{\alpha\beta(k)}$  and  $\tilde{\omega}_{e(k)}$  and the Lyapunov function (35) converge to zero. Hence, the adaptive EMF observer is stable. ■

In addition, from the speed estimation error (33) it is possible to write the following adaptive law

$$\hat{\omega}_{e(k+1)} = \frac{\hat{\omega}_{e(k)}}{1 + \frac{T_s^2}{2} \gamma \left\| \mathbf{e}_{\alpha\beta(k)} \right\|_2^2} - \frac{T_s \gamma (1 - h_3) \left( \tilde{\mathbf{e}}_{\alpha\beta(k)}^T \mathbf{J} \mathbf{e}_{\alpha\beta(k)} \right)}{1 + \frac{T_s^2}{2} \gamma \left\| \mathbf{e}_{\alpha\beta(k)} \right\|_2^2}. \quad (39)$$

Therefore, the rotor position can be estimated by

$$\hat{\theta}_{e(k+1)} = \tan^{-1} \left( -\frac{\hat{e}_{\alpha(k+1)}}{\hat{e}_{\beta(k+1)}} \right) - \delta \quad (40)$$

where

$$\delta = \tan^{-1} \left( \frac{\hat{\omega}_{e(k+1)}}{\omega_o} \right) + \angle \left( \frac{\tilde{e}(z)}{w(z)} \right)_{z=e^{jT_s \hat{\omega}_{e(k+1)}}} \quad (41)$$

compensates the phase shift of both LPF2 and DSM current observer.

#### IV. SENSORLESS CURRENT VECTOR CONTROLLER

The stator current are regulated by a proportional-integral controller, which compensates the windup effects resulted from the limited inverter DC voltage and the delay of digital implementation, as shown Fig. 6.

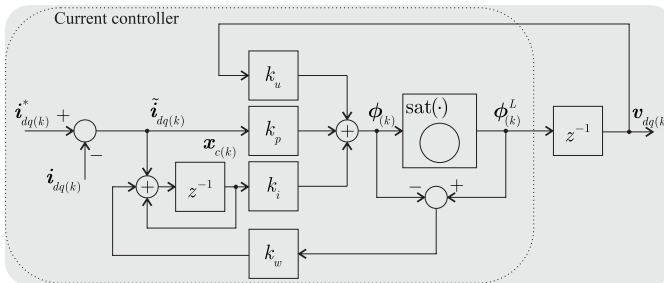


Fig. 6. PI current controller with anti-windup action and delay compensation. The identity matrix  $\mathbf{I}$  is omitted.

The controller is given by

$$\begin{aligned}\mathbf{x}_{c(k+1)} &= \mathbf{x}_{c(k)} + \tilde{\mathbf{i}}_{dq(k)} + k_w \mathbf{I} (\phi_{(k)}^L - \phi_{(k)}) \\ \mathbf{v}_{dq(k+1)} &= \phi_{(k)}^L \\ \phi_{(k)}^L &= \text{sat} \left( k_i \mathbf{I} \mathbf{x}_{c(k)} + k_p \mathbf{I} \tilde{\mathbf{i}}_{dq(k)} + k_u \mathbf{I} \mathbf{v}_{dq(k)} \right)\end{aligned}\quad (42)$$

where  $\mathbf{x}_{c(k)}$  is the state vector of the controller;  $k_i$ ,  $k_p$ ,  $k_u$  and  $k_w$  are integral, proportional, delay and anti-windup gains;  $\mathbf{I}$  is an identity matrix; the superscript  $L$  denotes limited vector, and  $\tilde{\mathbf{i}}_{dq(k)}$  and  $\mathbf{v}_{dq(k)}$  denote the tracking error and control action. The saturation function is defined by

$$\text{sat}(\phi_{(k)}) = \begin{cases} \phi_{(k)}, & \text{if } \|\phi_{(k)}\| \leq v_{\max}; \\ \frac{v_{\max}}{\|\phi_{(k)}\|} \phi_{(k)}, & \text{if } \|\phi_{(k)}\| > v_{\max} \end{cases} \quad (43)$$

where  $v_{\max}$  is the available DC voltage of the PWM converter. Appendix B gives a design procedure for the current controller.

#### V. EXPERIMENTAL RESULTS

A wind energy conversion system (WECS) emulation setup is used to validate the proposed sensorless vector controller. Fig. 7 and 8 show the experimental setup and the complete sensorless control scheme diagram block.

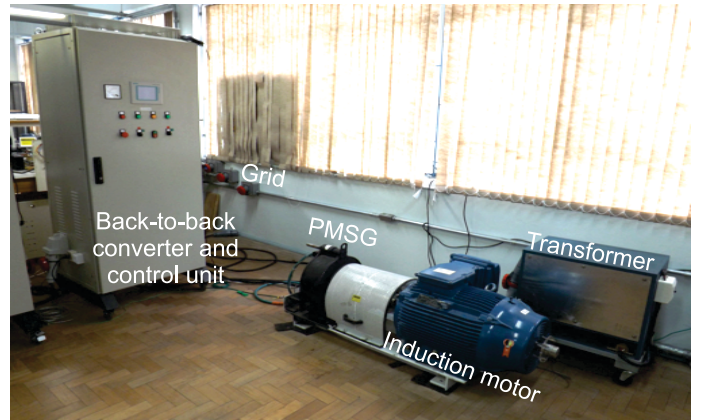


Fig. 7. Experimental setup.

Here, an induction motor (IM), which emulates a wind turbine, drives the PMSG. A back-to-back PWM converter connects the PMSG to the grid. The entire back-to-back PWM converter controller including the proposed sensorless scheme is implemented in a single DSPF28335. Space vector modulation is adopted with an asymmetrical switching sequence at 5 kHz resulting in a sampling frequency of 10 kHz. An AC580010AK42SGB absolute encoder provides the actual rotor position to quantify the position estimation error of the proposed sensorless scheme. The actual mechanical speed is obtained by differentiation of the measured position and it is used to quantify the speed estimation error. Table I gives the parameters of the PMSM.

Table I  
PARAMETERS OF THE PMSM.

Parameter	Value	Parameter	Value
Rated speed [rpm]	800	Pole number	24
Rated power [kW]	18	Magnet flux [Wb]	0.25
Rated torque [Nm]	216	Stator inductance [mH]	1.8
Rated current [A]	45	Stator resistance [ $\Omega$ ]	0.18

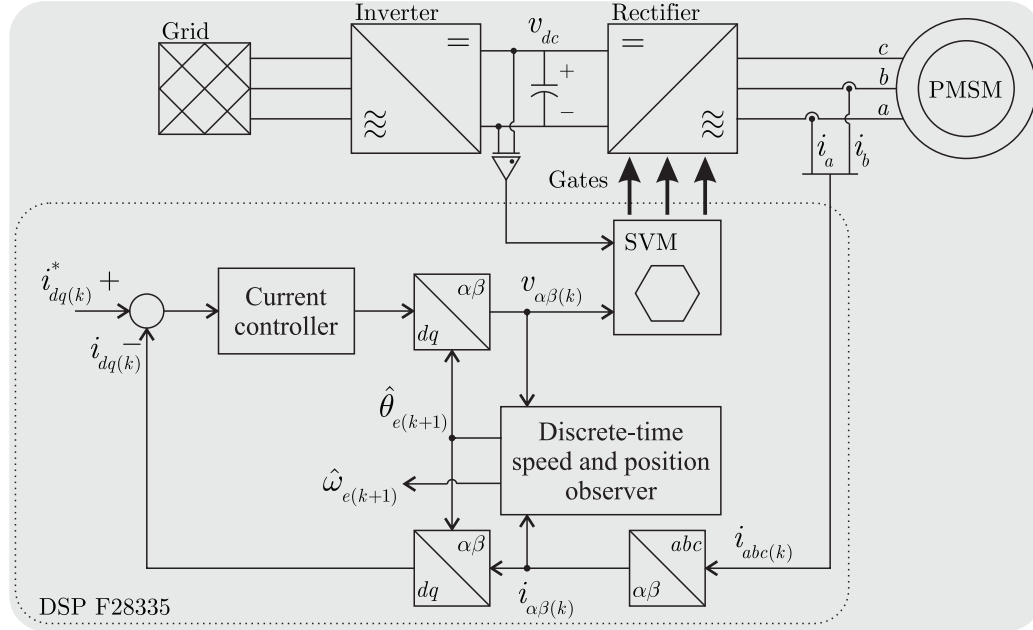


Fig. 8. Proposed sensorless vector control for PMSM.

The discrete-time speed and position observer is designed according to the Section III. Table II gives the observers gains, considering  $|w_{(k)}|_{\max} = 380V$  at 160 Hz and the LPF2 cutoff frequency equals 200 Hz. Concerning the gains of the EMF observer (32),  $h_3$  is selected within the range (0, 2) according to the Theorem 2 and  $\gamma$  is a positive gain, which provides a degree of freedom to adjust the transient response of the estimated speed.

Table II  
DISCRETE-TIME SPEED AND POSITION OBSERVER GAINS.

Gain	$h_1$	$h_2$	$h_3$	$\omega_{\text{cut}} [\text{Hz}]$	$\gamma$
Value	2	119	$9 \cdot 10^{-3}$	1342	10

The current controller is designed by linear quadratic regulator (LQR) methodology according to described in Appendix B. The controller gains are:  $k_p = 1.88$ ,  $k_i = 0.1$ ,  $k_u = -0.1$  and  $k_w = 10$ . In addition, the current reference  $i_{d(k)}^*$  is set in zero [41]. The maximum power point tracking control [42] determines the current reference  $i_{q(k)}^*$  as follows

$$i_{q(k)}^* = -k_{\text{opt}} \hat{\omega}_{m(k)}^2 \quad (44)$$

where  $k_{\text{opt}} = 7 \text{ mA} / (\frac{\text{rad}}{\text{s}})^2$  depends on the wind turbine characteristic and on the PMSG parameters.

In the following results, the variables  $\theta_{e(k)}$ ,  $\hat{\theta}_{e(k)}$  and  $\tilde{\theta}_{e(k)}$  denote actual and estimated position, and position estimation error;  $\omega_{m(k)}$ ,  $\hat{\omega}_{m(k)}$  and  $\tilde{\omega}_{m(k)}$  are actual and estimated mechanical speed, and mechanical speed estimation error;  $\sigma_{\alpha(k)}$  and  $\sigma_{\beta(k)}$  denotes the sliding functions of  $\alpha\beta$ -axes;  $i_{d(k)}$  and  $i_{q(k)}$  are synchronous currents of the PMSG;  $\sigma^*$  and  $\sigma_{\max}$  denote

the equilibrium and maximum theoretical values to the sliding functions. In addition,  $\hat{\theta}_{e(k)}$  is normalized.

Fig. 9 and 10 demonstrate the steady state performance of the proposed speed and position observer. They show the actual and estimated value of both speed and position as well as the position estimation error with mechanical speed of 5, 400 and 800 rpm. Fig. 9 shows that the proposed sensorless control can operate in speeds close to zero, i.e., less 1% than the rated rotor speed. Moreover, its performance improves as the speed increases, as shown Fig. 10. Fig. 11 enlarges Fig. 10, demonstrating the effectiveness of the proposed sensorless control.

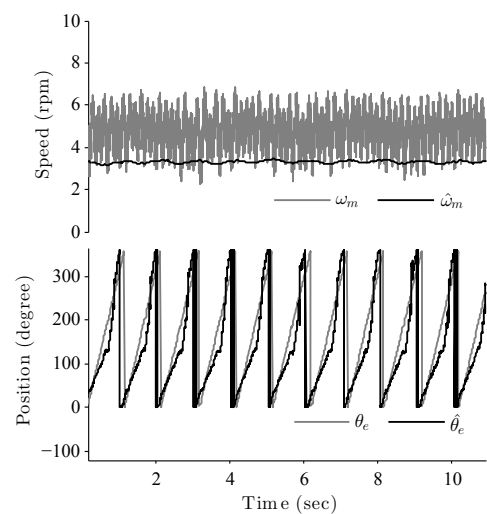


Fig. 9. Experimental results. Top: actual  $\omega_{m(k)}$  and estimated  $\hat{\omega}_{m(k)}$  mechanical speed; Bottom: actual  $\theta_{e(k)}$  and estimated  $\hat{\theta}_{e(k)}$  rotor position at low speed, 5 rpm.

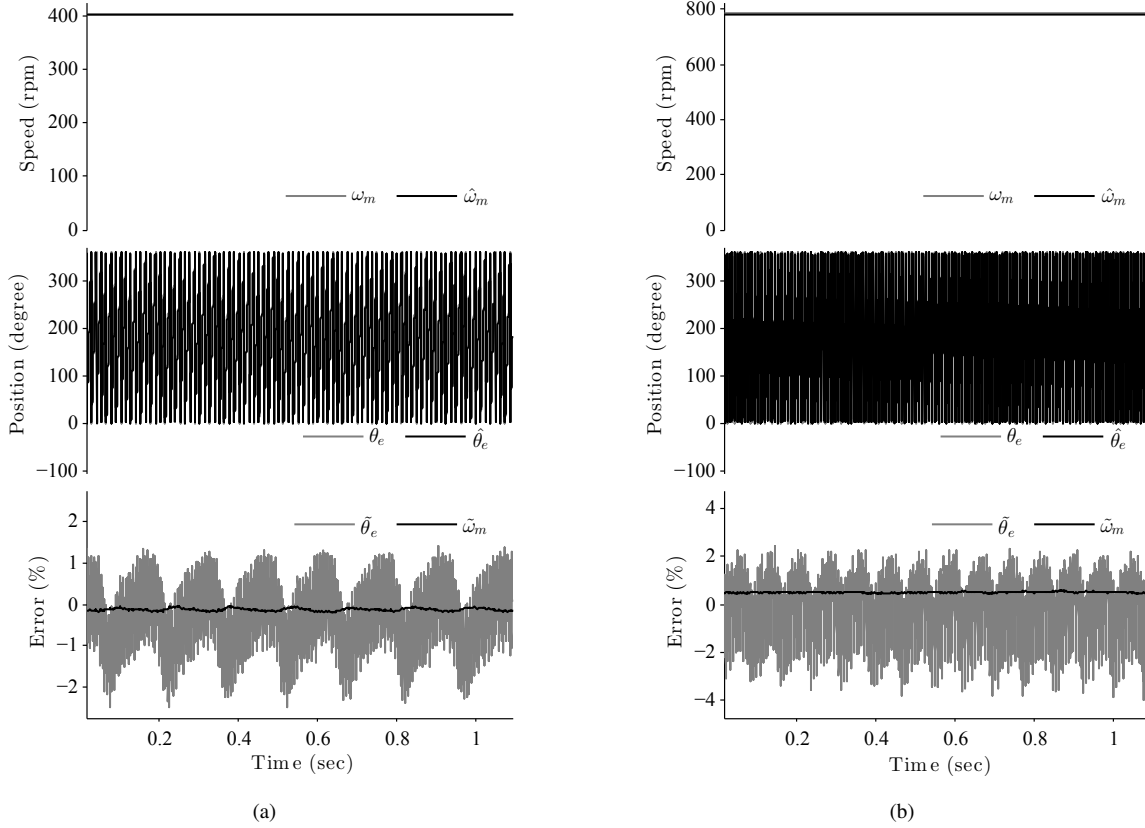


Fig. 10. Experimental results: (a) 400 and (b) 800 rpm. Top: actual  $\omega_{m(k)}$  and estimated  $\hat{\omega}_{m(k)}$  mechanical speed; Middle: actual  $\theta_{e(k)}$  and estimated  $\hat{\theta}_{e(k)}$  rotor position; Bottom: percentage estimation error of the position  $\hat{\theta}_{e(k)}$  and mechanical speed  $\hat{\omega}_{m(k)}$ .

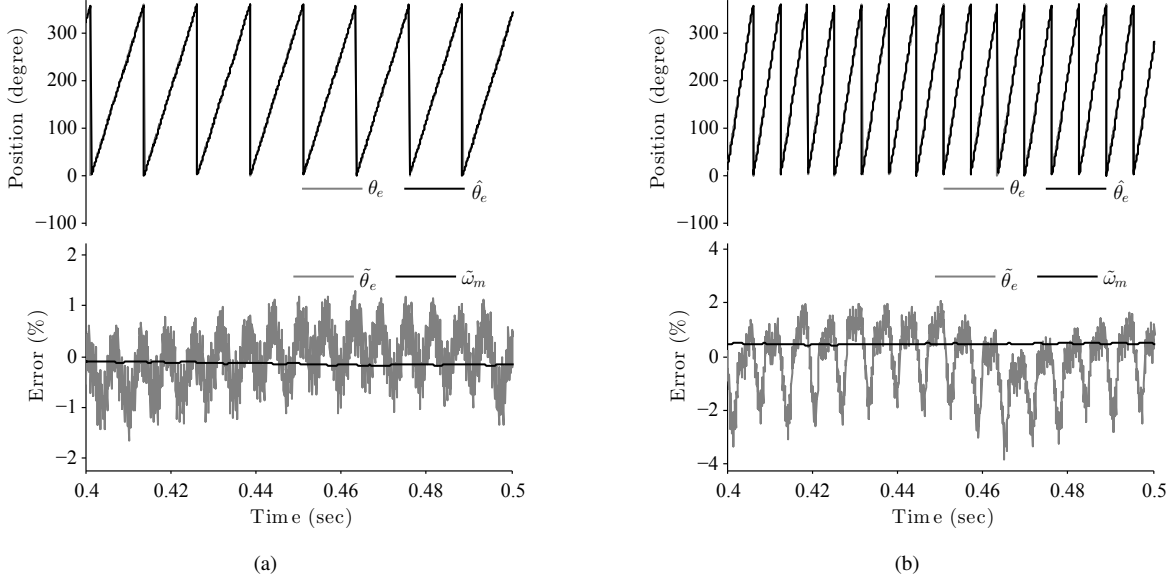


Fig. 11. Enlargement of Fig. 10: (a) 400 and (b) 800 rpm. Top: actual  $\theta_{e(k)}$  and estimated  $\hat{\theta}_{e(k)}$  rotor position and Bottom: percentage estimation error of the position  $\hat{\theta}_{e(k)}$  and mechanical speed  $\hat{\omega}_{m(k)}$ .

Fig. 12 shows the sliding functions obtained from the DSP memory at speeds: 5, 400 and 800 rpm. Observe that the quasi-

sliding motion is assured across the surface  $\sigma_{\alpha\beta(k)} = 0$  in accord with Section III-B. The equilibrium  $\sigma^*$  correlates with

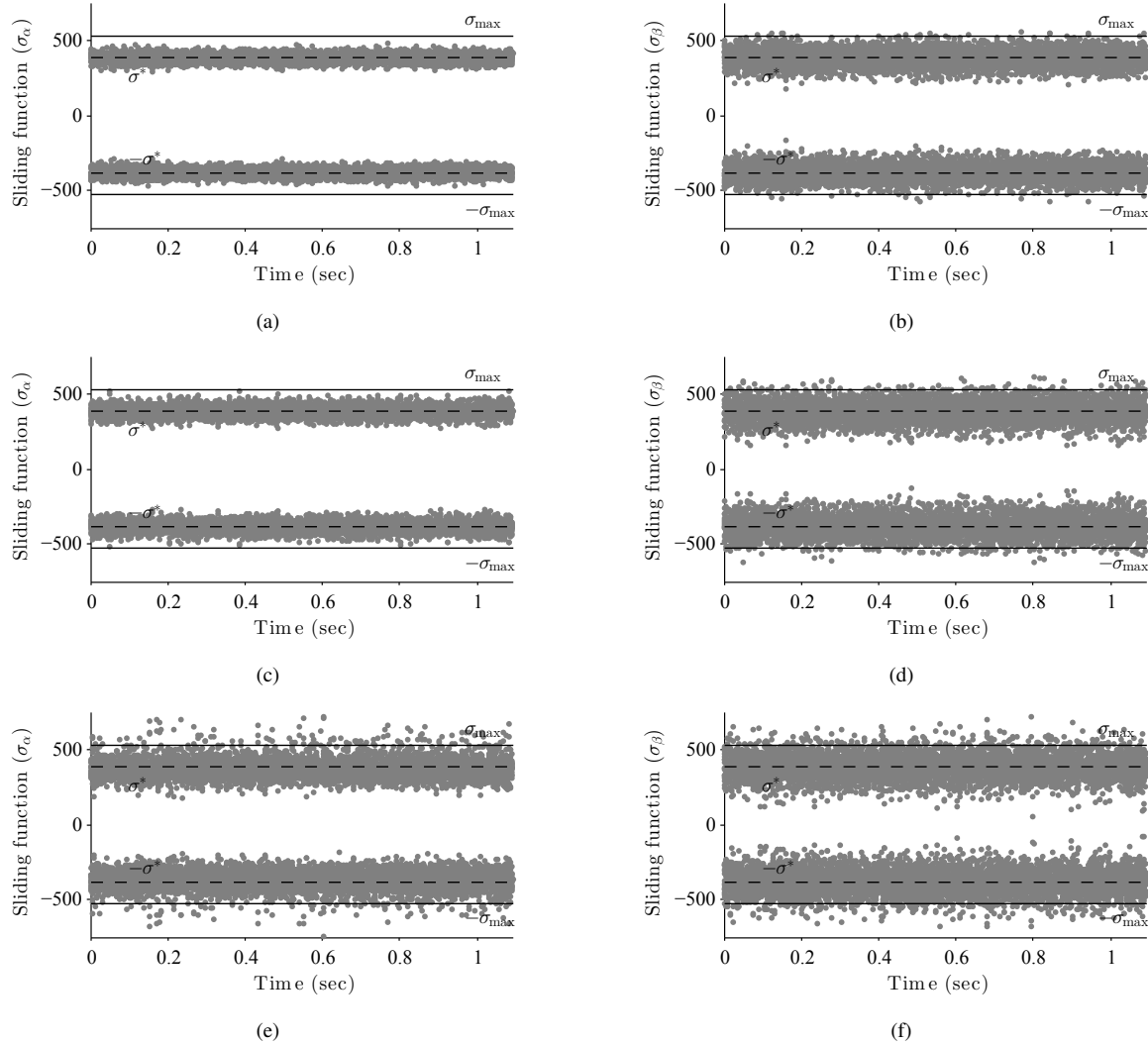


Fig. 12. Experimental result. Sliding functions  $\sigma_{\alpha\beta(k)}$ : (a) and (b) for 5 rpm; (c) and (d) for 400 rpm, and (e) and (f) for 800 rpm.

the experimental equilibrium if the perturbation  $w_{(k)}$  is null or small, as shown Fig. 12(a) and 12(b). These results demonstrate that the influence of the perturbation  $w_{(k)}$  on the sliding function becomes noticeable at the high speed range. Although the experimental sliding function exceeds the  $\sigma_{\max}$  in some sampling instants, which is attributed to measurement noises, PWM and EMF harmonics, the experimental results validate the theoretical predictions, as shown Fig. 12(e) and 12(f).

Fig. 13 shows the sliding function  $\sigma_{\beta(k)}$  for two distinct values of the gain  $h_2$ . In Fig. 13(a),  $h_2$  is obtained according to the proposed design procedure and its value is given in Table II. On the other hand, in Fig. 13(b), the gain is changed to a value that violates the proposed methodology. These results demonstrate that proposed design procedure ensures the quasi-sliding motion since the  $\sigma_{\beta(k)}$  crosses the sliding plane  $\sigma = 0$  at every and each sampling instant. Hence, the chattering holds a predictable behaviour.

Fig. 14 shows the calculated  $e_{\alpha(k)}$  and estimated  $\hat{e}_{\alpha(k)}$  EMF at speeds: 5, 400 and 800 rpm. Note that the actual EMF

is unavailable and the calculated EMF is determined by (2) using the actual rotor position  $\theta_{e(k)}$  and speed  $\omega_{e(k)}$ . Thus, the calculated EMF can be considered the fundamental component of the actual EMF if the speed is kept constant. Fig. 14(a) shows that the estimated EMF  $\hat{e}_{\alpha(k)}$  follows the calculated EMF  $e_{\alpha(k)}$  at low speed, 5 rpm. The EMF distortion is mainly attributed to the speed oscillations resulted from the generator-motor coupling and from the non-linearities on the motor drive. On the other hand, Fig. 14(b) and 14(c) show the calculated  $e_{\alpha(k)}$ , the estimated  $\hat{e}_{\alpha(k)}$  as well as the estimated EMF with phase compensation (41),  $\hat{e}_{\alpha(k)}^{CP}$ , at speed 400 rpm and 800 rpm. Observe that the phase compensation allows an effective rotor position estimation in wide speed range as demonstrated in Fig. 9, 10 and 11.

Fig. 15 and 16 show the close-loop behavior of the proposed sensorless control. The mechanical speed increases from 5 to 800 rpm, decreases to 400 rpm and returns to 5 rpm in a rate of 9 rpm/s. As soon as the speed reaches 1% of the rated speed, the estimation errors decrease significantly as the speed

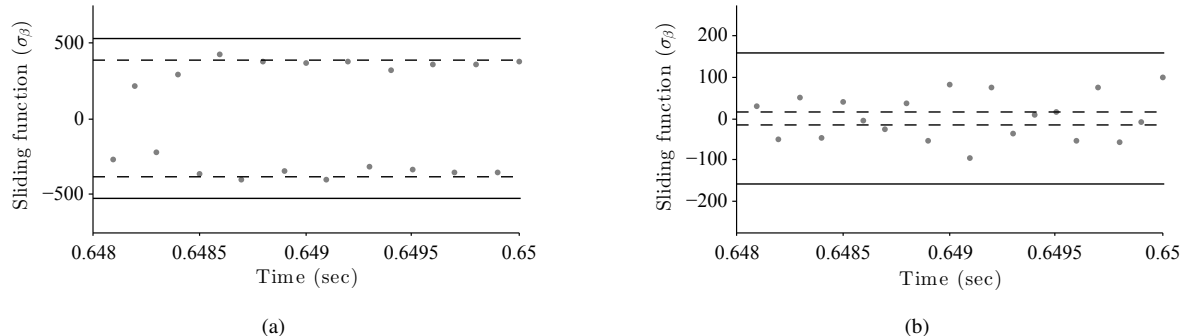


Fig. 13. Experimental results. Sliding function  $\sigma_{\beta(k)}$ : (a)  $h_2 = 119$ , which follows the proposed design procedure, and (b)  $h_2 = 5$ , which violates the DSM attributes.  $\omega_m(k) = 400$  rpm.

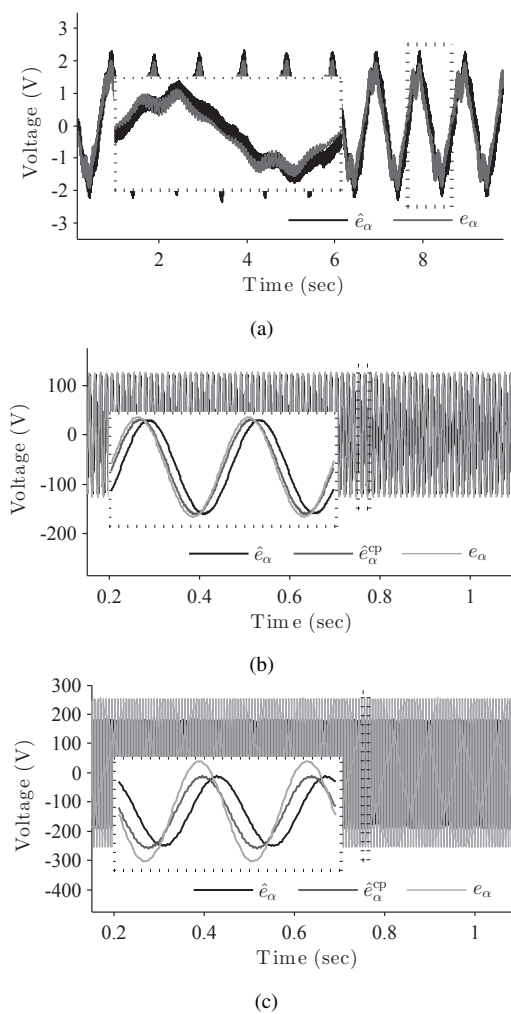


Fig. 14. Experimental result: (a) for 5 rpm, (b) for 400 rpm and (c) for 800 rpm. EMF: calculated  $e_{\alpha(k)}$ , estimated  $\hat{e}_{\alpha(k)}$  and estimated with phase compensation  $\hat{e}_{\alpha(k)}^{cp}$ .

increases. In addition, Fig. 16 shows that the stator currents follow their references as expected. Fig. 15 (bottom) reveals a small position and speed estimation errors in steady state,

except for speeds near zero. Even in speeds close to zero the proposed sensorless control ensures an acceptable performance for the system, as shown in Fig. 16.

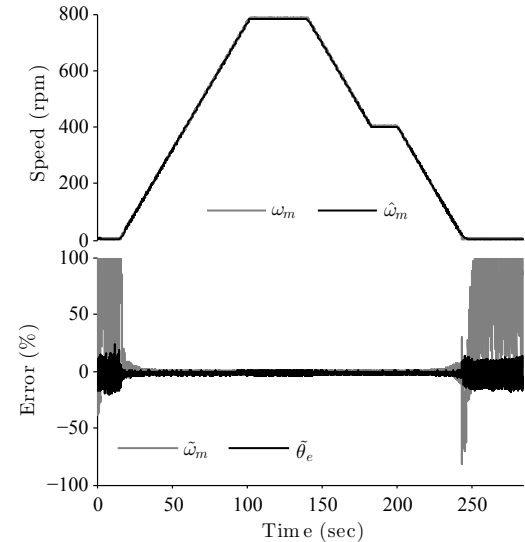


Fig. 15. Experimental results. Top: actual  $\omega_{m(k)}$  and estimated  $\hat{\omega}_{m(k)}$  mechanical speed; Bottom: percentage estimation error of the position  $\hat{\theta}_{e(k)}$  and mechanical speed  $\hat{\omega}_{m(k)}$  under variable speed: increases from 5 to 800 rpm, decreases to 400 rpm and returns to 5 rpm.

Fig. 17 shows current transient due to steps in the reference  $i_{q(k)}$ . The estimated speed undergoes transient and it converges for the actual value in steady state. Fig. 18 enlarges the Fig. 17 around the first step. Note that the estimated rotor position  $\hat{\theta}_{e(k)}$  remains very close to the actual position during the current transition.

Even though the obtained results consider a WECS application, Fig. 19 shows motor reversal from 300 to -300 rpm to demonstrate the performance of the proposed speed estimation. Observe that the estimation error is close to zero.

During the experiments, the measured stator voltages have been used to reduce the impact of the PWM rectifier nonlinearities such as the dead-time and semiconductors voltage drops [43]. Blaabjerg *et al.* [44] provide several techniques

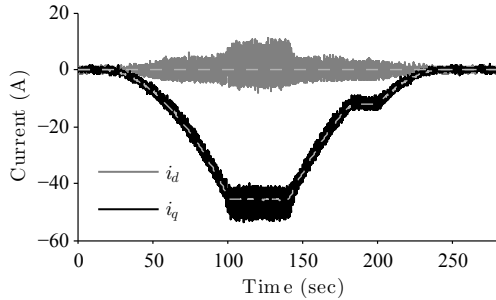


Fig. 16. Experimental results. Stator current  $i_{dq(k)}$  in synchronous frame under variable speed: increases from 5 to 800 rpm, decreases to 400 rpm and returns to 5 rpm.

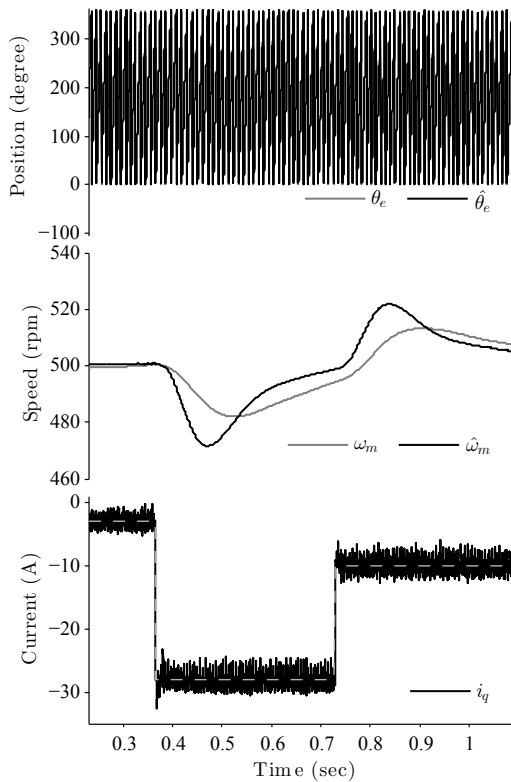


Fig. 17. Experimental results. Top: actual  $\theta_{e(k)}$  and estimated  $\hat{\theta}_{e(k)}$  rotor position; Middle: actual  $\omega_{m(k)}$  and estimated  $\hat{\omega}_{m(k)}$  mechanical speed; Bottom: current  $i_{q(k)}$ . Operation under variable load at 500 rpm.

to compensate the nonlinearities inverter like: the dead-time, the load dependent DC-link voltage ripple and the voltage drop across the switches. These techniques can be used in the proposed sensorless control to avoid additional voltage sensors.

## VI. CONCLUSION

A sensorless vector control is proposed for a permanent magnet synchronous machine, which consists in the discrete time speed and position observer and a current controller. The former comprises of the discrete-time sliding mode current observer and of the discrete-time adaptive EMF observer. It is

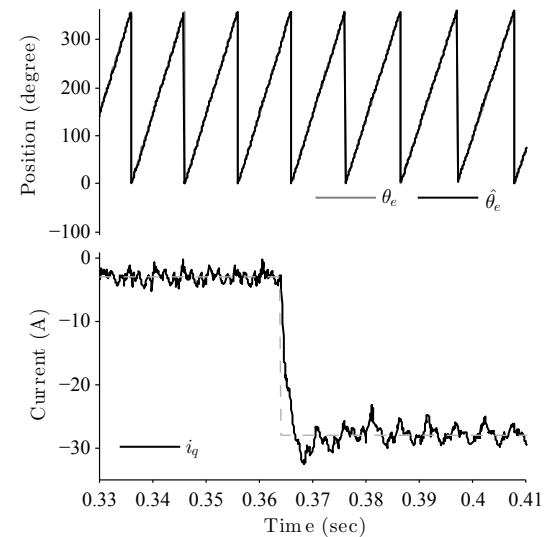


Fig. 18. Enlargement of Fig. 17. Top: actual  $\theta_{e(k)}$  and estimated  $\hat{\theta}_{e(k)}$  rotor position; Bottom:  $i_q$  current, considering the first current step. Operation under variable load at 500 rpm.

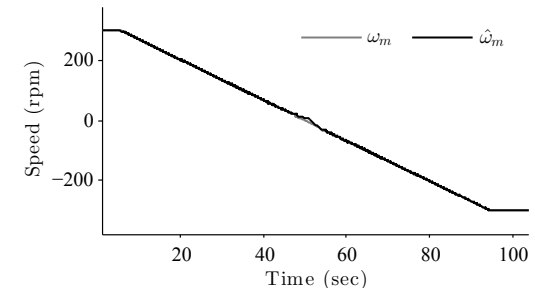


Fig. 19. Experimental results. Actual  $\omega_{m(k)}$  and estimated  $\hat{\omega}_{m(k)}$  mechanical speed under motor reversal.

demonstrated both theoretically and experimentally that quasi-sliding mode can be ensured under bounded perturbations. In addition, a discrete-time adaptive EMF observer is proposed by Lyapunov's direct method providing both the speed and estimated rotor position. Experimental results validate the proposed sensorless control, demonstrate its performance, and validate the proposed design procedure. They are carried out for a wind energy conversion system, however the proposed sensorless algorithm can be considered for other applications.

## ACKNOWLEDGMENT

The authors would like to thank for CAPES and for CNPq by financial support.

## APPENDIX A EXAMPLE TO DESIGN PROCEDURE OF THE DSM CURRENT OBSERVER

The design procedure comprise two steps. The first computes the gains  $h_1$  and  $\omega_{cut}$ . The second determines the gain  $h_2$ . The

input parameters consist of: the initial values  $h_{1\text{initial}}$ ,  $h_{2\text{initial}}$  and  $\omega_{\text{cutinitial}}$ ; the final values  $h_{1\text{final}}$ ,  $h_{2\text{final}}$  and  $\omega_{\text{cutfinal}}$ ; the search step  $\Delta_1$ ,  $\Delta_2$  and  $\Delta_3$ ; the maximum  $\lambda_{\max}$  and the minimum  $\lambda_{\min}$  eigenvalues of  $\mathbf{G}^2$ ; the maximum absolute value  $w_{\max}$  and frequency  $f_{w_{\max}}$  of the perturbation  $w_{(k)}$  and the sampling period  $T_s$ . Thus, define

$$\begin{aligned} h_1 &= h_{1\text{initial}} : \Delta_1 : h_{1\text{final}}, \\ h_2 &= h_{2\text{initial}} : \Delta_2 : h_{2\text{final}}, \\ \omega_{\text{cut}} &= \omega_{\text{cutinitial}} : \Delta_3 : \omega_{\text{cutfinal}} \text{ and} \end{aligned} \quad (45)$$

the functions:  $\text{eig}(\cdot)$  that returns the eigenvalues of a matrix;  $\text{find}(\cdot)$  that returns the indices of a matrix or a vector;  $f_1(\cdot, \cdot, \cdot, \cdot)$  that is (27), and  $f_2(\cdot, \cdot, \cdot, \cdot)$  that is (26). Fig. 20 provides a pseudo-code to the first step. To achieve the second step, the values  $h_{1\text{opt}}$ ,  $\omega_{\text{cutopt}}$ ,  $g_{1\text{opt}}$  and  $g_{2\text{opt}}$  are used according to Fig. 21. Therefore, the gains  $h_{1\text{opt}}$ ,  $h_{2\text{opt}}$  and  $\omega_{\text{cutopt}}$  denote the desired gains that ensure the quasi-sliding mode.

```

1: for  $i \leftarrow 1 : \text{length}(h_1)$  do
2:   for  $j \leftarrow 1 : \text{length}(\omega_{\text{cut}})$  do
3:      $g_{12} \leftarrow f_1(h_{1(i)}, \omega_{\text{cut}(j)}, f_{w_{\max}}, T_s)$ 
4:      $g_{1(i,j)} \leftarrow g_{12(1)}$ 
5:      $g_{2(i,j)} \leftarrow g_{12(2)}$ 
6:      $\lambda_{G^2} \leftarrow |\text{eig}(\mathbf{G}^2(h_{1(i)}, \omega_{\text{cut}(j)}, T_s))|$ 
7:     if  $\max(\lambda_{G^2}) > \lambda_{\max}$  or  $\min(\lambda_{G^2}) < \lambda_{\min}$  then
8:        $g_{1(i,j)} \leftarrow 10^5$ 
9:        $g_{2(i,j)} \leftarrow 10^5$ 
10:    end if
11:   end for
12:  end for
13:   $(i_{\text{opt}}, j_{\text{opt}}) \leftarrow \text{find}(\min(g_1 + g_2))$ 
14:   $h_{1\text{opt}} \leftarrow h_{1(i_{\text{opt}})}$ 
15:   $\omega_{\text{cutopt}} \leftarrow \omega_{\text{cut}(j_{\text{opt}})}$ 
16:   $g_{1\text{opt}} \leftarrow g_{1(i_{\text{opt}}, j_{\text{opt}})}$ 
17:   $g_{2\text{opt}} \leftarrow g_{2(i_{\text{opt}}, j_{\text{opt}})}$ 

```

Fig. 20. Pseudo-code for the first design step of the DSM current observer.

## APPENDIX B

### DESIGN PROCEDURE OF THE CURRENT CONTROLLER

The continuous-time dynamic behaviour of a nonsalient PMSM in synchronous reference frame  $dq$  with the magnetic flux can be obtained from (1), given by

$$\dot{\mathbf{i}}_{dq} = \Phi \mathbf{i}_{dq} + \Gamma \mathbf{v}_{dq} - \Gamma \mathbf{e}_{dq} \quad (46)$$

where  $\mathbf{i}_{dq}$ ,  $\mathbf{v}_{dq}$  and  $\mathbf{e}_{dq}$  denote vectors of stator currents and voltages, and induced electromotive force (EMF) in  $dq$ -frame. Here, the matrix  $\Phi$  is given by

$$\Phi = \begin{bmatrix} -\frac{R_s}{L_s} & \omega_e \\ -\omega_e & -\frac{R_s}{L_s} \end{bmatrix} \quad (47)$$

where  $\omega_e$  is the rotor speed. Therefore, the discrete-time dynamic behaviour of a nonsalient PMSM can be expressed as

$$\mathbf{i}_{dq(k+1)} = \mathbf{A} \mathbf{i}_{dq(k)} + \mathbf{B} \mathbf{v}_{dq(k)} - \mathbf{B} \mathbf{e}_{dq(k)}. \quad (48)$$

```

1: for  $i \leftarrow 1 : \text{length}(h_2)$  do
2:    $x_{12}^* \leftarrow |f_2(h_{1\text{opt}}, \omega_{\text{cutopt}}, h_{2(i)}, T_s)|$ 
3:    $x_1^* \leftarrow x_{12}^*(1)$ 
4:    $x_2^* \leftarrow x_{12}^*(2)$ 
5:    $x_{1\max(i)} \leftarrow x_1^* + g_{1\text{opt}} w_{\max}$ 
6:    $x_{2\max(i)} \leftarrow x_2^* + g_{2\text{opt}} w_{\max}$ 
7:    $r_1 \leftarrow x_1^* - g_{1\text{opt}} w_{\max}$ 
8:    $r_2 \leftarrow x_2^* - g_{2\text{opt}} w_{\max}$ 
9:   if  $r_1 < 0$  or  $r_2 < 0$  then
10:     $x_{1\max(i)} \leftarrow 10^5$ 
11:     $x_{2\max(i)} \leftarrow 10^5$ 
12:   end if
13:  end for
14:   $i_{\text{opt}} \leftarrow \text{find}(\min(x_{1\max} + x_{2\max}))$ 
15:   $h_{2\text{opt}} \leftarrow h_{2(i_{\text{opt}})}$ 

```

Fig. 21. Pseudo-code for the second design step of the DSM current observer.

If the reference current is constant and control action  $\mathbf{v}_{dq(k)}$  remains in the linear region, i.e.  $i_{dq(k+1)}^* = i_{dq(k)}^*$  and  $\phi_{(k)}^L = \phi_{(k)}$ , then from (42) and (48), the discrete-time closed-loop model can be written as

$$\xi_{(k+1)} = (\mathbf{A}_{ol} - \mathbf{B}_{ol} \mathbf{K}) \xi_{(k)} + \mathbf{E} \mathbf{e}_{dq(k)} \quad (49)$$

where  $\xi_{(k)} = [\tilde{\mathbf{i}}_{dq(k)}^T \quad \mathbf{x}_{c(k)}^T \quad \mathbf{v}_{dq(k)}^T]^T$  denotes the augmented state vector and the matrices  $\mathbf{A}_{ol}$ ,  $\mathbf{B}_{ol}$ ,  $\mathbf{K}$  and  $\mathbf{E}$  are determined by

$$\begin{aligned} \mathbf{A}_{ol} &= \begin{bmatrix} \mathbf{A} & \mathbf{0} & -\mathbf{B} \\ \mathbf{I} & \mathbf{I} & \mathbf{0} \\ \mathbf{0} & \mathbf{0} & \mathbf{0} \end{bmatrix}, & \mathbf{E} &= [\mathbf{B}^T \quad \mathbf{0} \quad \mathbf{0}]^T \text{ and} \\ \mathbf{B}_{ol} &= [\mathbf{0} \quad \mathbf{0} \quad \mathbf{I}]^T, & \mathbf{K} &= -[k_p \mathbf{I} \quad k_i \mathbf{I} \quad k_u \mathbf{I}]. \end{aligned} \quad (50)$$

Several design techniques can be used to compute the gain matrix  $\mathbf{K}$  and to ensure the stability, for example: linear matrix inequalities [45], pole placement and LQR. In addition, the gain  $k_w$  can be selected as  $1/k_i$ .

## REFERENCES

- [1] J. Holtz, "Sensorless control of induction machines – with or without signal injection?" *IEEE Transactions on Industrial Electronics*, vol. 53, no. 1, pp. 7–30, feb. 2005.
- [2] P. Acarnley and J. Watson, "Review of position-sensorless operation of brushless permanent-magnet machines," *IEEE Transactions on Industrial Electronics*, vol. 53, no. 2, pp. 352 – 362, april 2006.
- [3] M. Pacas, "Sensorless drives in industrial applications," *IEEE Industrial Electronics Magazine*, vol. 5, no. 2, pp. 16–23, june 2011.
- [4] M. J. Corley and R. D. Lorenz, "Rotor position and velocity estimation for a salient-pole permanent-magnet synchronous machine at standstill and high speeds," *IEEE Transactions on Industry Applications*, vol. 34, no. 4, pp. 784–789, 1998.
- [5] S. Ogasawara and H. Akagi, "Implementation and position control performance of a position-sensorless IPM motor drive system based on magnetic saliency," *IEEE Transactions on Industry Applications*, vol. 34, no. 4, pp. 806–812, 1998.
- [6] N. Bianchi and S. Bolognani, "Influence of rotor geometry of an IPM motor on sensorless control feasibility," *IEEE Transactions on Industry Applications*, vol. 43, no. 1, pp. 87–96, 2007.

- [7] N. Bianchi, S. Bolognani, J.-H. Jang, and S.-K. Sul, "Advantages of inset PM machines for zero-speed sensorless position detection," *IEEE Transactions on Industry Applications*, vol. 44, no. 4, pp. 1190–1198, 2008.
- [8] F. Briz and M. Degner, "Rotor position estimation," *IEEE Industrial Electronics Magazine*, vol. 5, no. 2, pp. 24–36, june 2011.
- [9] R. Wu and G. Slemon, "A permanent magnet motor drive without a shaft sensor," *IEEE Transactions on Industry Applications*, vol. 27, no. 5, pp. 1005–1011, sep/oct 1991.
- [10] S. Bolognani, M. Zigliotto, and M. Zordan, "Extended-range PMSM sensorless speed drive based on stochastic filtering," *IEEE Transactions on Power Electronics*, vol. 16, no. 1, pp. 110–117, 2001.
- [11] M. Rashed, P. F. A. MacConnell, A. F. Stronach, and P. Acarnley, "Sensorless indirect-rotor-field-orientation speed control of a permanent-magnet synchronous motor with stator-resistance estimation," *IEEE Transactions on Industrial Electronics*, vol. 54, no. 3, pp. 1664–1675, 2007.
- [12] K.-Y. Lian, C.-H. Chiang, and H.-W. Tu, "LMI-based sensorless control of permanent-magnet synchronous motors," *IEEE Transactions on Industrial Electronics*, vol. 54, no. 5, pp. 2769–2778, oct. 2007.
- [13] A. Piippo, M. Hinkkanen, and J. Luomi, "Analysis of an adaptive observer for sensorless control of interior permanent magnet synchronous motors," *IEEE Transactions on Industrial Electronics*, vol. 55, no. 2, pp. 570–576, 2008.
- [14] M. Singh and A. Chandra, "Application of adaptive network-based fuzzy inference system for sensorless control of PMSG-based wind turbine with nonlinear-load-compensation capabilities," *IEEE Transactions on Power Electronics*, vol. 26, no. 1, pp. 165–175, jan. 2011.
- [15] R. Ortega, L. Praly, A. Astolfi, J. Lee, and K. Nam, "Estimation of rotor position and speed of permanent magnet synchronous motors with guaranteed stability," *IEEE Transactions on Control Systems Technology*, vol. 19, no. 3, pp. 601–614, may 2011.
- [16] T. Furuhashi, S. Sangwongwanich, and S. Okuma, "A position-and-velocity sensorless control for brushless DC motors using an adaptive sliding mode observer," *IEEE Transactions on Industrial Electronics*, vol. 39, no. 2, pp. 89–95, apr 1992.
- [17] Z. Chen, M. Tomita, S. Doki, and S. Okuma, "New adaptive sliding observers for position- and velocity-sensorless controls of brushless DC motors," *IEEE Transactions on Industrial Electronics*, vol. 47, no. 3, pp. 582–591, jun 2000.
- [18] Y.-S. Han, J.-S. Choi, and Y.-S. Kim, "Sensorless PMSM drive with a sliding mode control based adaptive speed and stator resistance estimator," *IEEE Transactions on Magnetics*, vol. 36, no. 5, pp. 3588–3591, sep 2000.
- [19] Z. Yan, C. Jin, and V. Utkin, "Sensorless sliding-mode control of induction motors," *IEEE Transactions on Industrial Electronics*, vol. 47, no. 6, pp. 1286 – 1297, dec 2000.
- [20] R. McCann, M. Islam, and I. Husain, "Application of a sliding-mode observer for position and speed estimation in switched reluctance motor drives," *IEEE Transactions on Industry Applications*, vol. 37, no. 1, pp. 51–58, jan/feb 2001.
- [21] C. Lascu, I. Boldea, and F. Blaabjerg, "Comparative study of adaptive and inherently sensorless observers for variable-speed induction-motor drives," *IEEE Transactions on Industrial Electronics*, vol. 53, no. 1, pp. 57 – 65, feb. 2005.
- [22] S. Chi, Z. Zhang, and L. Xu, "Sliding-mode sensorless control of direct-drive PM synchronous motors for washing machine applications," *IEEE Transactions on Industry Applications*, vol. 45, no. 2, pp. 582–590, 2009.
- [23] G. Foo and M. Rahman, "Sensorless sliding-mode MTPA control of an IPM synchronous motor drive using a sliding-mode observer and HF signal injection," *IEEE Transactions on Industrial Electronics*, vol. 57, no. 4, pp. 1270–1278, april 2010.
- [24] H. Kim, J. Son, and J. Lee, "A high-speed sliding-mode observer for the sensorless speed control of a PMSM," *IEEE Transactions on Industrial Electronics*, vol. 58, no. 9, pp. 4069–4077, 2011.
- [25] W. Qiao, X. Yang, and X. Gong, "Wind speed and rotor position sensorless control for direct-drive PMG wind turbines," *IEEE Transactions on Industry Applications*, vol. 48, no. 1, pp. 3–11, 2012.
- [26] Z. Qiao, T. Shi, Y. Wang, Y. Yan, C. Xia, and X. He, "New sliding-mode observer for position sensorless control of permanent-magnet synchronous motor," *IEEE Transactions on Industrial Electronics*, vol. 60, no. 2, pp. 710–719, 2013.
- [27] M. Hamida, J. De Leon, A. Glumineau, and R. Boisliveau, "An adaptive interconnected observer for sensorless control of pm synchronous motors with online parameter identification," *IEEE Transactions on Industrial Electronics*, vol. 60, no. 2, pp. 739–748, 2013.
- [28] G. Wang, R. Yang, and D. Xu, "DSP-based control of sensorless IPMSM drives for wide-speed-range operation," *IEEE Transactions on Industrial Electronics*, vol. 60, no. 2, pp. 720–727, feb 2013.
- [29] G. Wang, Z. Li, G. Zhang, Y. Yu, and D. Xu, "Quadrature PLL-based high-order sliding-mode observer for IPMSM sensorless control with online MTPA control strategy," *IEEE Transactions on Energy Conversion*, vol. 28, no. 1, pp. 214–224, 2013.
- [30] R. Morales-Caporal, E. Bonilla-Huerta, M. Arjona, and C. Hernandez, "Sensorless predictive DTC of a surface-mounted permanent-magnet synchronous machine based on its magnetic anisotropy," *IEEE Transactions on Industrial Electronics*, vol. 60, no. 8, pp. 3016–3024, 2013.
- [31] V. Utkin, "Sliding mode control design principles and applications to electric drives," *IEEE Transactions on Industrial Electronics*, vol. 40, no. 1, pp. 23–36, feb 1993.
- [32] V. Utkin, J. Guldner, and M. Shishkin, *Sliding Mode Control in Electromechanical Systems*. CRC Press, 1999.
- [33] S. Sarpturk, Y. Isteftanopoulos, and O. Kaynak, "On the stability of discrete-time sliding mode control systems," *IEEE Transactions on Automatic Control*, vol. 32, no. 10, pp. 930 – 932, oct 1987.
- [34] H. Sira-Ramirez, "Nonlinear discrete variable structure systems in quasi-sliding mode," *Int. J. Control.*, vol. 54, no. 5, pp. 1171–1187, oct 1991.
- [35] G. Michaletzky and L. Gerencser, "BIBO stability of linear switching systems," *IEEE Transactions on Automatic Control*, vol. 47, no. 11, pp. 1895–1898, 2002.
- [36] J. Daafouz and J. Bernussou, "Poly-quadratic stability and  $H_\infty$  performance for discrete systems with time varying uncertainties," in *Proc. 40th IEEE Conf. Decision and Control*, vol. 1, 2001, pp. 267–272.
- [37] I. Boiko, L. Fridman, A. Pisano, and E. Usai, "Analysis of chattering in systems with second-order sliding modes," *IEEE Transactions on Automatic Control*, vol. 52, no. 11, pp. 2085–2102, 2007.
- [38] M. Bernardo, C. Budd, A. R. Champneys, and P. Kowalczyk, *Piecewise-smooth Dynamical Systems: Theory and Applications*, 1st ed., ser. Applied Mathematical Sciences, S. Antman, J. Marsden, and L. Sirovich, Eds. Springer, December 2007, vol. 163.
- [39] A. Aroudi, M. Debbat, and L. Martinez-Salamero, "Poincaré maps modeling and local orbital stability analysis of discontinuous piecewise affine periodically driven systems," *Nonlinear Dynamics*, vol. 50, pp. 431–445, 2007.
- [40] W. Gao, Y. Wang, and A. Homaifa, "Discrete-time variable structure control systems," *IEEE Transactions on Industrial Electronics*, vol. 42, no. 2, pp. 117 – 122, apr 1995.
- [41] R. Krishnan, *Permanent Magnet Synchronous and Brushless DC Motor Drives*. CRC Press, 2009.
- [42] A. Yazdani and R. Iravani, "A neutral-point clamped converter system for direct-drive variable-speed wind power unit," *IEEE Transactions on Energy Conversion*, vol. 21, no. 2, pp. 596–607, 2006.
- [43] H. Zhao, Q. M. J. Wu, and A. Kawamura, "An accurate approach of nonlinearity compensation for VSI inverter output voltage," *IEEE Transactions on Power Electronics*, vol. 19, no. 4, pp. 1029–1035, 2004.
- [44] F. Blaabjerg, J. K. Pedersen, and P. Thoegersen, "Improved modulation techniques for PWM-VSI drives," *IEEE Transactions on Industrial Electronics*, vol. 44, no. 1, pp. 87–95, 1997. [Online]. Available: <http://ieeexplore.ieee.org/stamp/stamp.jsp?arnumber=557503>
- [45] S. Boyd, L. E. Ghaoui, E. Feron, and V. Balakrishnan, *Linear Matrix Inequalities in System and Control Theory*, ser. Studies in Applied Mathematics. Philadelphia - PA: Society for Industrial and Applied Mathematics (SIAM), 1994, vol. 15.



**Thiago Bernardes** was born in Natal - RN, Brazil, in 1983. He received his B.Sc. degree in Electrical Engineering from the Federal University of Ceará (2007), Master and D.Sc. degrees in Electrical Engineering from Federal University of Santa Maria (2009 and 2013).

He works with the Power Electronics and Control Research Group (GEPOC). His research interests include: sliding mode control, wind energy conversion systems and control applied to power electronics systems.



**Vinícius Foleto Montagner** got his PhD (2005) and post-doctoral degrees in Electrical Engineering from University of Campinas (2006). Currently, he is a professor at Federal University of Santa Maria, and works with the Power Electronics and Control Research Group (GEPOC). His research interests include control theory and applications.



**Hilton Abílio Gründling** Hilton Abílio Gründling was born in Santa Maria, RS, Brazil, in 1954. He received the B.Sc. degree from the Pontifical Catholic University of Rio Grande do Sul, Porto Alegre, Brazil, in 1977, the M.Eng. degree from the Federal University of Santa Catarina, Santa Catarina, Brazil, in 1980 and the D.Sc. degree from the Technological Institute of Aeronautics, São Paulo, Brazil, in 1995. Since 1980, he has been with the Federal University of Santa Maria, Rio Grande do Sul, Brazil, where he is currently a Titular Professor. His research interests include robust model reference adaptive control, discrete control and control systems applications.



**Humberto Pinheiro** was born in Santa Maria, Brazil, in 1960. He received the B.Sc. degree from the Federal University of Santa Maria, Santa Maria, Brazil, in 1983, the M.Eng. degree from the Federal University of Santa Catarina, Florianópolis, Brazil, in 1987, and the Ph.D. degree from Concordia University, Montreal, QC, Canada, in 1999.

From 1987 to 1990, he was a Research Engineer with a Brazilian UPS company and then joined the Pontifícia Universidade Católica do Rio Grande do Sul, Brazil, where he lectured on power electronics. Since 1991, he has been with Federal University of Santa Maria. His current research interests include grid-connected three-phase converters, wind energy conversion systems, and control applied to power electronics systems. Dr. Pinheiro is currently a member in the IEEE Power Electronics and IEEE Industrial Electronics Society.